Hydrogen-induced cracking and corrosion behavior of friction stir welded plates of API 5L X70 pipeline steel

J. M. Giarola[1]; J. W. Calderón-Hernández[2]; J.M Quispe-Avilés [2]; *J.A. Avila[3]; W. W. Bose Filho[1]

1. USP – University of São Paulo, Av. Trabalhador São Carlense 400, São Carlos, SP, 13566590, Brazil.
2. USP – University of São Paulo, Av. Prof. Luciano Gualberto, 380 - Butantã, São Paulo - SP, 05508-010, Brazil
3. UNESP – São Paulo State University (UNESP), Campus of São João da Boa Vista, São João da Boa Vista, SP, Brazil.

*Corresponding author: Prof. Dr. Julian A. Avila D. julian.avila@unesp.br, +55 19 36382432, Av. Profª Isette Corrêa Fontão, 505, Jardim das Flores, 13876-750 - São João da Boa Vista, SP, Brazil.

Abstract

The use of friction stir welding (FSW) has proven to be an excellent alternative to join engineering components. Although FSW has had a significant development in recent years, challenges for new applications have been raised, such as offshore steel parts suffering hydrogen embrittlement in the gas and oil industry. Therefore, in this work, the microstructure, corrosion, and hydrogen-induced cracking were investigated in a two-pass FSW welded joint of API 5L X70 pipeline steel. The electrochemical results indicate an inhibitory effect on corrosion reaction because of a carbonate product generation in the steel surface. The polygonal ferritic and degenerated pearlite bands microstructure in the base metal fixed carbonate deposits in the steel surface. In the welded regions, the bainitic microstructure and the carbide particle distribution are less efficient in setting the weld surface carbonate deposit. HIC tests showed cracks initiation and propagation to be more prone in hard phases.

Keywords: friction stir welding; FSW; corrosion resistance; potentiodynamic polarization tests; electrochemical microcell, LEIS, HIC, API 5L X70

1. Introduction

As API 5L X70, high-strength steel has been applied in pipelines to transport oil and gas. The API steels offer a high ratio of strength and toughness [1]. These pipes need to be welded to construct long-distance pipeline projects, electric arc welding being the most conventional method [2]. Due to the welding process, the microstructure of base metal will modify significantly in the welded zone. Implementing Friction Stir Welding (FSW) in steels will replace the pipelines fusion welding process [3–5]. The FSW is a solid-state joining process

obtained through thermomechanical processing of the base metal-induced a rotating, non-consumable tool [3–7]. Among the many advantages of using FSW in the pipeline industry, reducing energy consumption up to 60% to 80% and problems associated with solidification are reduced or even eliminated [7,8]. Technology development focused on full-scale friction welding systems for pipeline steels is already being studied [7,9,10].

During the transportation of oil and gas, corrosion and hydrogen-induced cracking (HIC) are likely to cause unexpected accidents. Hydrogen sulfide (H_2S) and carbon dioxide (CO_2) are the most common dissolved gases present in oil and gas deposits, causing corrosion in pipelines [11,12]. Consequently, the welded region corrosion behavior differs from the metal base [12–15]. Comparing fusion welding and friction stir welding (FSW), the former has improved productivity and quality [16,17]. FSW can create a complex microstructure and increase mechanical properties [18]; however, the FSW can remain unaltered or even improve the corrosion resistance [19–21].

The environmental influence in external pipeline corrosion, being varied, may contain different chloride, sulfate, bicarbonate, and carbonate concentration [22]. Thus, the corrosion resistance is worth studying in the high-strength low-alloy steels (HSLA) and their welded joints. Corrosion susceptibility increases due to the metallurgical changes and residual stresses introduced [14,23–25]. In an aerated carbonate solution, the microstructure can be associated with the material corrosion, in which the bainite structures do not form a passive film as the ferritic [22]. Another factor that can influence corrosion in this environment is stress. More carbonate product is generated in the region with compressive stress, causing decreased dissolution more significantly than tensile stress [26].

Few authors have studied how the FSW process affects low carbon steel corrosion properties. Da Cruz et al. [19] studied the corrosion behavior in the API-X70 friction stir weld zones in an acidic medium. The stir zone was more anodic than the base metal, composed of banded microstructures ferrite and pearlite. On the other hand, the most cathodic region was the thermo-mechanically affected zone, consisting of acicular ferrite, bainite, and martensite-austenite constituent. In the case of 3.5 % NaCl solution, the FSW joint presents the increase of corrosion resistance after microstructural changes, as grain refinement [20,21], which led to homogenization in those regions [21]. Behjat et al. [27] showed that the severity of attack BM was higher than that observed in SZ due to the high deriving force of galvanic corrosion because to the presence of the coarse microstructure and ferrite/pearlite structure, unlike of the SZ in which that the grain refinement, in the ferrite in bainite structure, during the FSW process decreased the galvanic corrosion. However, Husain et al. [28] reported a lower corrosion resistance in the weld nugget than the base metal in medium strength steel due to ferrite grain size, second-phase fraction, the relative fraction of high and low-angle grain

boundaries, fraction of Coincidence Site Lattice (CSL) boundaries, and residual strain. In which different corrosion mechanisms occurred, in the MB the corrosion attack was uniform, in contrary the weld nugget that occurred corrosion for pit.

In the process of hydrogen-induced cracking, the hydrogen atoms can diffuse in steel and are trapped into reversible and irreversible sites that combine to make hydrogen molecules. An increase in the pressure is caused by hydrogen molecule accumulation inside the void, creating crack initiations [29]. The most common trapped are precipitated, inclusions, lattice defects such as micro-voids, vacancies, dislocations, grain boundaries, and stress concentration regions [30–33].

The cracks in the presence of hydrogen can initiate mainly in Si- and Al oxide-enriched inclusions [30]. The inclusions shape facilitates HIC propagation, primarily the spinal and rectangular inclusions in smaller grains and shorter distances between these [34]. The microstructure influences the crack initiation, with hard products such as martensite and bainite prone to HIC [33]. In contrast, the acicular ferrite had excellent resistance due to its high toughness, preventing crack propagation [32]. The other factor raising HIC susceptibility is the segregation zones, in which areas with a high concentration of Mn, Si, and S elements, tended to uptake hydrogen and initiate cracks [29]. The effect of the grain size on hydrogen diffusion is complex because it influences mobility and permeability in different ways. In a sample with small grain sizes, the hydrogen mobility increases due to a more prominent grain boundary area per unit volume; however, the overall permeability decreases due to higher density of nodes or junction points that can act as traps for hydrogen atoms [35,36]. Other than that, another controversial feature that affects the HIC is the grain boundary. Some authors indicate the large-angle grain boundary acts as an irreversible hydrogen trap improving the resistance to hydrogen-induced cracking, which impedes hydrogen diffusion to the crack tip [37]. However, other studies showed that large-angle grain boundaries due to relatively high internal energy are considered preferred places for crack propagation [38,39].

Few studies have reported hydrogen-induced cracking effects on FSW welded joints of pipeline steels. Although, some authors suggested that residual hydrogen levels of welded joints for FSW not increased during dry and underwater welding [3,40]. Thus, the FSW reduces the risk of HIC in comparison to conventional fusion welding processes. Unlike in traditional welding, several studies showed the HIC effect [35,37,41,42]. Gan et al. [41] studied the X100 pipeline steel with submerged-arc welding. A higher trap density of irreversible hydrogen and inhomogeneous microstructure in the weded joint caused more susceptibility to the HIC of base metal. Being that the inclusions of Al, Ca, Si, Mn acted as preferential places for an initiate of HIC cracks. Kang et al.[42], assessed the HIC susceptibility in the coarse-grained heat-affected zone in three types of carbon steel. The microstructure of the steels was similar and

consisted mainly of bainite and martensite. However, the difference in prior austenite grain boundaries (PAGBs) was the determining factor in HIC susceptibility. The microstructure composed of few PAGBs caused low HIC susceptibility due to the formation of primary ferrite.

Most of the HIC and corrosion studies of welded low carbon steels involve conventional welding processes based on the fusion of the material. Therefore, the literature on how the FSW process affects low carbon steel corrosion properties and hydrogen-induced cracking is scarce, especially in pipelines. Thus in this work, the HIC and corrosion behavior of the X70 steel friction stir welded joint was investigated to simulate the pipeline environmental condition by combining localized electrochemical impedance spectroscopy (LEIS) and potentiodynamic polarization tests. Different regions in the welded joint were studied, i.e., heat affected zone (HAZ), stirred zone (SZ), and even base metal (BM). We found that the different microstructures delivered different corrosion behavior in the bicarbonate/carbonate solution and HIC. The microstructure of BM, polygonal ferritic, and degenerated pearlite bands present better corrosion and HIC behavior.

2. Experimental procedure

Plates of API-5L-X70, 18 mm in thickness, were used to construct two-pass FSW bead-on-plate joints. The chemical composition of this steel is shown in Table 1. The chemical analysis was carried out using optical emission spectrometer ANACOM brad B2Advanced.

Table 1. Chemical composition of the API 5L X70 steel (weight %).

C	Si	Mn	P	S	Cr	Ni	Mo	Nb	V	Ti
0.009	0.19	1.59	0.010	0.003	0.02	0.21	0.04	0.055	0.046	0.011

2.1. Microstructural characterizations

The passes were oriented perpendicular to the rolling direction of the original plate. The FSW tool was composed of a metallic matrix composite, PCBN–WRe, 25%Re–W alloy reinforced with 60%vol PCBN (Polycrystalline Cubic Boron Nitride). Such tools possessed a 9.5 mm long threaded conical pin and a convex threaded shoulder. It used a force control mode with 39 kN, a spindle speed of 300 RPM, and a transverse speed of 100 mm min^{-1}.

The base material and weld regions microstructural characterization was conducted using optical microscopy (OM) and scanning electron microscopy (SEM). The Electron Backscattering diffraction (EBSD) detector coupled in a Quanta 650 FEG SEM available at LNNano, Campinas. Sample cross-sections were prepared using conventional methods for metallographic preparation. Samples were ground from 100-grit up to 1200-grit SiC paper, polished with a diamond paste of 3 µm, 1 µm, and finished with colloidal silica. For SEM

analysis, the samples were etched Nital 2% was used to reveal the grain boundaries. The SEM images were used to identify the microstructural zones of grains and ferrite plate sizes, bainite packet morphology. For the acquisition of the EBSD maps, no etching procedure was used. The EBSD maps provided information about the microstructure crystallographic orientation, grain size, and grain boundaries misorientation grains. The step size used in EBSD analysis was 0.25 µm, and the analyzed areas were approximately 150 µm X 126 µm.

2.2. LEIS experiments

LEIS experiments in the mapping mode (LEIM) were carried out using a commercial Ametek® VS-LEIS system, controlled with the VerScan® Software. The scanned area was 1.6 cm^2, and the maps were obtained with a perturbation amplitude of 30 mV (rms) and a step size of 40 µm. The experiments were conducted in 0.05M Na2CO3, 0.1M NaHCO3, and 0.1M NaCl, with a pH of 9.6 alkaline solution [26] using an Ag/AgCl electrode as the reference and a Pt ring as the counter electrode. Diagrams were regularly acquired up to 24 h of immersion.

2.3. Electrochemical tests

The electrochemical tests, potentiodynamic polarization was performed in a three-electrode cell through a potentiostat. The BM and weld joint samples of X70 pipeline steel were used as a working electrode, a silver/silver chloride (Ag/AgCl) as a reference electrode, and a platinum wire as the auxiliary electrode. Before the potentiodynamic tests, the open circuit potential (OCP) was registered for 30 min to achieve the stationary state. The polarization started from -100 mV concerning the OCP with a scan rate of 1 mV/s until it reaches 10^{-3} A/cm^2 or 200 mV.

A microcell arrangement with a 2mm diameter o-ring gasket was used to conduct electrochemical measurements in small regions, thus permitting the selection of each microstructural part of the welded joint separately, such as BM, HAZ (advancing side (HAZ-AS), and retreating side (HAZ-RS)), SZ. At least three potentiodynamic polarization tests were done in every zone, and the resulting summary of the curves was discussed.

2.4. Hydrogen induced cracking (HIC) experiments

Hydrogen induced cracking experiment was accomplished in H_2S-saturated A solution(0.5% acetic acid (wt) + 5.0% NaCl (wt)) and followed the recommendations of NACE TM0284-11[43]. The specimens were extracted from the rolling direction with (100 ± 1) mm length and (18 ± 1) mm width. In contrast, the thicknesses corresponded to those of the original plate, extracted from the rolling direction, and were cut from the BM and FSweld steel plates. These samples were ground with grit paper up to sandpaper 320-grit and ultrasonically

degreased with acetone, according to the NACE TM0284-11[43] recommendations. Figure 1 shows the tested schematic specimen diagram and the surfaces observed after the experiment in the BM and FSWeld.

After the HIC test, the samples were withdrawn from the vessel and washed with soap/water, washed with ethanol, and dried. Finally, the specimens were sectioned with a precision cutter machine with a diamond-like disk, then embedded in bakelite with the cross-sections facing upwards. Next, samples were ground up to sandpaper 1200-grit and polished with a diamond paste of 1 μm. The crack initiation and propagation were studied by OM (Olympus BX60M), and SEM (OlympusPhilips XL-30) analyzed with and without Nital 2% etching. The value of crack sensitivity ratio (CSR), crack length ratio (CLR), and crack thickness ratio (CTR) was calculated according to the following equations [43]:

$$CSR = \frac{\sum(a x b)}{(W x T)} \; x100\% \tag{1}$$

$$CLR = \frac{\sum a}{W} \; x100\% \tag{2}$$

$$CTR = \frac{\sum b}{T} \; x100\% \tag{3}$$

In which *a* is the cracking length, *b* represents the crack thickness, *W* represents the width, and *T* the specimen thickness.
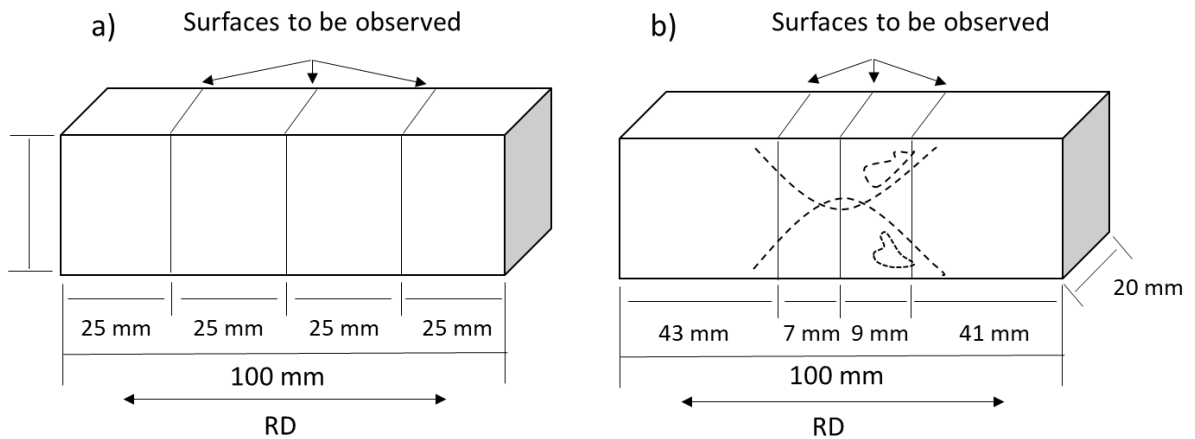

Figure 1: Schematic diagram of the specimen for the HIC experiment and the surfaces to be observed. (a) BM, (b) FSWeld showing the macrostructural regions, the stir zone, and the hard zone is enclosed in the dashed lines.

3. Results and discussion

3.1. Microstructural Characterization

The severe thermomechanical cycle applied to the steel by FSW resulted in a different microstructure composition in each FSW region than the base metal, as depicted in Figure 2. Figure 2a presents the cross-section micrograph that revealed the weld regions: the stir zone (SZ) and heat-affected zone (HAZ). The SZ can also be subdivided into three: stir zone (SZ), hard zone (HZ), and re-stirred zone (RSZ). The HAZ was subdivided into two areas: high temperature (HAZ–HT) and low temperature (HAZ–LT).
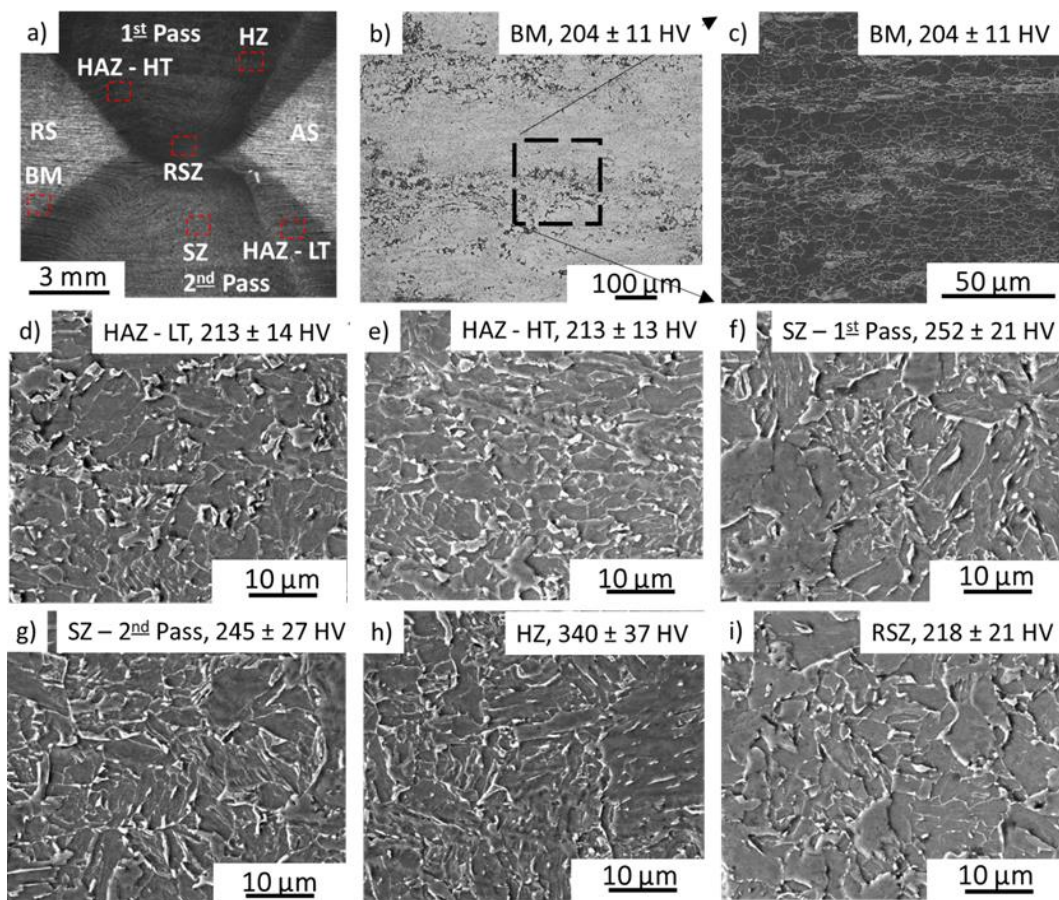
Figure 2: Optical and SEM micrographs showing the macro and microstructures of the FSW API X70 steel. (a) Macrography showing the cross-section of the FSWelded joint; (b) and (c) BM; (d) HAZ-LT; (e) HAZ- HT; (f) SZ-1st pass; (g) SZ-2nd Pass; (h) HZ; (i) RSZ.

The base metal (BM) depicted a combination of equiaxed and polygonal ferritic grains and degenerated pearlite bands, shown in Figure 2b and c. The microstructure of the HAZ-LT was mainly composed of polygonal ferrite (Figure 2d). At the HAZ-HT, bainite packets with straight ferrite plates, granular bainite, and acicular ferrite are observed (Figure 2e). The SZ depicted granular bainite and bainite packets with irregular and straight ferrite plates (Figure

2f-g). The HZ results in creating a lath-type structure containing much more bainite packets with straight plates than granular bainite (Figure 2h). The RSZ is formed by the overlap of FSW passes. Due to the double stirring, this region suffers re-heating and deformation, changing its microstructure twice. This heat flux caused austenitization and recrystallization, resulting in a predominantly polygonal ferrite microstructure (Figure 2i) with many secondary phases. This classification is in agreement with previous works [44,45].

Figure 3 shows Inverse Pole Figures (IPF) for the weld joint regions processed from the EBSD data, which was performed to reveal grain boundary misorientation distribution.
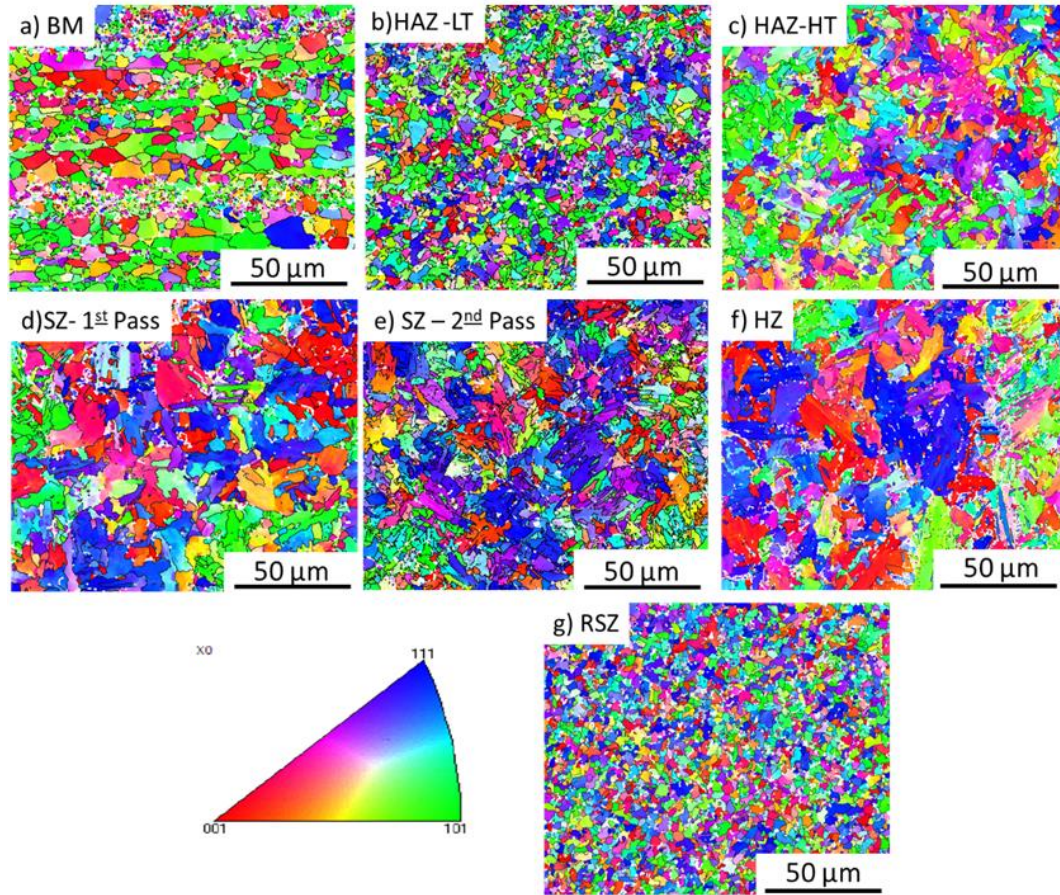

Figure 3: Electron backscatter diffraction (EBSD) for microstructural characterization of the FSW API X70 steel. (a) BM; (b) HAZ-LT; (c) HAZ-HT; (d) SZ in the 1st Pass; (e) SZ in the 2nd pass; (f) HZ; (g) RSZ.

Table 2 summarizes the correlated misorientation angles of each region shown in Figure 3 and Figure 4. The welded joint areas, i.e., HAZ-HT, SZ from the 1st pass, SZ from the 2nd pass, and HZ, had their highest proportion of misorientation angles below 15°. Bainite packet boundaries correspond to the boundaries with misorientation angles above 45° [46]. A high frequency of misorientation angles distribution between 40° and 60° are related to the orientation of individual bainitic laths [47]. In addition, misorientations between bainitic packets

8

formed from the same austenite grain are associated with peaks around 55° [48]. The bainite packet boundaries are more frequent in the welded joints regions, attributed to the thermal and stirring effects [46].
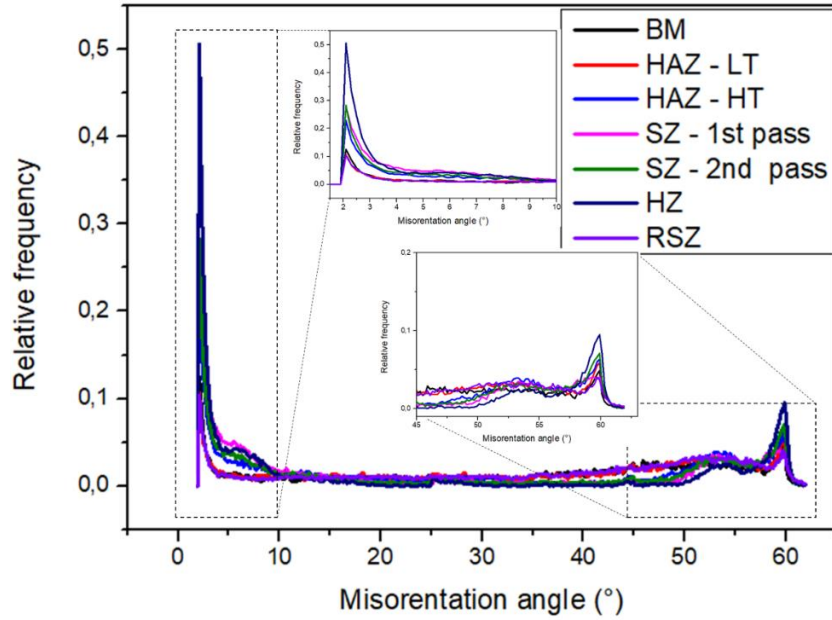

Figure 4. Misorientation angle distribution of the welded regions.

Table 2: Summary of effective misorientation, EBSD processed results.

Zone	Hardness (HV)	Frequency (%)			
		< 15°	>15°and <45°	>45° and <60°	>60°
BM	204 ± 11	22	37	39	1
HAZ-LT	213 ±13	21	35	42	2
HAZ-HT	213 ± 14	41	19	39	1
SZ - 1st pass	252 ± 21	53	14	31	2
SZ - 2nd pass	245 ± 27	47	15	36	2
HZ	340 ± 14	62	6	31	1
RSZ	218 ± 21	19	37	43	1

The grain size and the quantified second phase in each region were reported in previous work [21] and are summarized in Figure 5. It is possible to observe a grain refinement compared with the base metal . During the FSW processing, the steel suffered high plastic deformation combined with elevated temperature, leading to dynamic recrystallization and grain refinement [15,19,20,49]. The second phase is composed of carbides, degenerated pearlite, M/A, and cementite [47]. This second phase is present in all areas, being the region

stir zone with the smallest grains. Examining Figure 5 is possible to verify a large amount of the second phase. Thus, the misorientation pattern shown in Figure 4 in this range may have been caused by the presence second phase and the formation of ferrite and bainite from adjacent austenite grains.
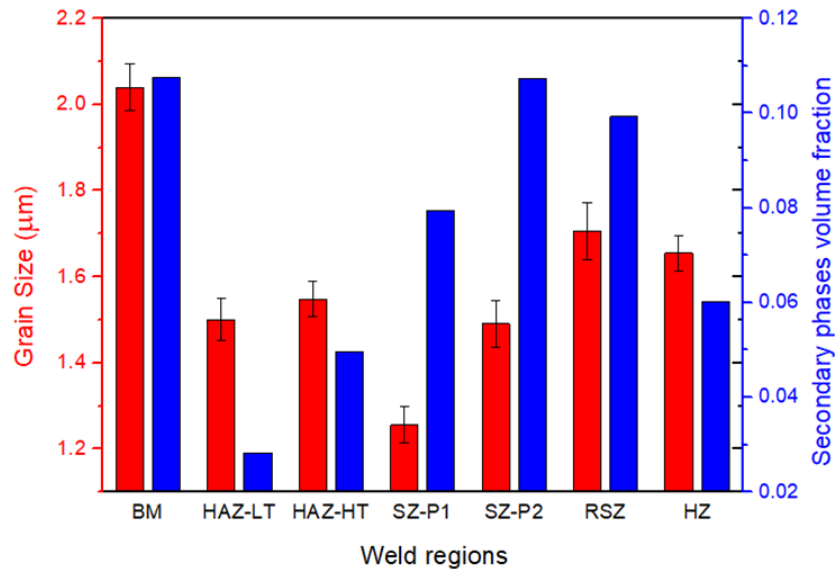

Figure 5. Grain size and Second Phases relative to each weld region. Data modified from [21].

The EBSD analysis indicates that grain boundary misorientations are of high angles (15° to 45°). A common depicted crystallographic characteristic in Figure 4 is the absence of misorientations between 20° and 47°, related to EBSD analysis conducted inside large prior austenite grains and the character of the austenite-to-ferrite transformation inside the prior austenite [50–52]. However, misorientations in this range result from phase transformation from different austenite grains [48,50]. The second phase can also be responsible for this range of misorientation angles. Gurova et al. [53] find peaks for cementite and retained austenite range from 30° for 45°, while Odnobokova et al. [54] found peaks around 45°; they correlated this angle to the martensitic transformation. Shakhova et al. [55] related that misorientations of 42.9° and 46° are boundaries between austenite and martensite.

The BM, HAZ-LT, and RSZ present similar misorientation. The microstructure of polygonal ferrite (PF), Figures 3a, b,and g, formed by more randomly oriented grains, is subgrain boundaries with low angle surrounded by high angle grain boundaries [56].

The acicular ferrite (AF) presented in HAZ-HT and HZ, Figure 3c and f, is constituted for ferrite grains with interwoven and irregular shapes [46]. This structure has a needle-shaped structure that nucleates non-metallic inclusions distributed in welding joint parts. It displays a

higher proportion of high-angle and a significant number of low-angle grain boundaries [56–58]. The great misorientation reflects the nucleating heterogeneously from non-metallic inclusions, creating a higher proportion of high-angle grain boundaries [56,58].

The granular bainite (GB) is found in HAZ-HT, SZ, and HZ, defined as an aggregation of subgrains composed of irregular ferrite with second phases distributed between the irregular ferrite grains. The second phases are a small island of M/A and pearlite [47,57,59]. The misorientation is more random with a broad peak in high angle >40° concerning boundaries between granular bainite and M/A. In contrast, the sub-grain boundaries inside the granular bainitic grains show a low angle relation of <20° [47,57].

Bainite packets (BP) can be found with straight and irregular plates [46] and were detected in the SZ, HZ, and HAZ-HT, mostly straight (thin bainite packets) at the hard zone and stir zone of the second passe and irregular (thick bainite packets) at the stir zone in the first passe and heat-affected-zone. This structure consists of packets of parallel ferrite plates or subgrains connected [56] with carbide particles cementite and inter-lath M/A constituents inside [57,59]. The material had a very high proportion of low-angle grains below 10° relative to the sub-grains and two smaller peaks in high angle grain boundaries relative to the packets of lath-type microstructure [48,56,57]. The difference between straight and irregular plates occurs by the different cooling rates [59,60]. Because of the overlap of the two weld passes, the first-pass suffers the second pass heat effects, making the microstructure more irregular. All regions of the join, excluding HAZ-LT and RSZ, have clear peaks between 5° and 20°, another two peak between 50° and 60°, Figure 4. This peak is due to the high amounts of acicular ferrite and bainite [56,61]. The sample has a much higher peak at the low-angle range and smaller peaks above 50°, suggesting it has less acicular ferrite and more bainite [56].

3.2.   Hydrogen embrittlement results

Figure 6 shows images containing the micro-cracks at the cross-section mid-thickness in the weld regions and metal base. Table 3 shows all HIC parameters, including CSR, CLR, and CTR, calculated with Equations (1)–(3) for the BM, HAZ-HT, and SZ.

The HIC parameters in the weld regions were higher than BM values, meaning the weld regions were highly susceptible to HIC, being that HZA-HT presented higher values than SZ. (Table 3). For HAZ-HT, CLR, CTR, and CSR values are 94.13%, 19.67%, and 5.43%, respectively, which are larger than the acceptable criteria of 15.0%, 5.0%, and 2.0% by NACE TM0284-11 standard [43]. The BM and SZ were just not accepted by the CLR criteria.

The HIC results imply that BM exhibits better resistance than weld regions against HIC. This result depends on the following factors: inclusions, microstructure. The BM is composed

of ductile phases, grain size, being that BM has low grain boundary concentration due to the grain size average, as shown in Figure 5.

In the analyzed sample surface, the HIC cracks appeared at the center of the cross-section. In the rolling direction, in Figure 6a and b, in both samples, the microstructural characterizations previously realized exhibited that segregation bands are usually present in the mid-thickness of the plate. According to the literature, during hot-rolled steel making, elements with low melting points are accumulated to the center of the plate thickness. This rolling process feature delivers a plate with inhomogeneous distribution of elements along the cross-section, forming hard phases and undesired product formation [62–64].
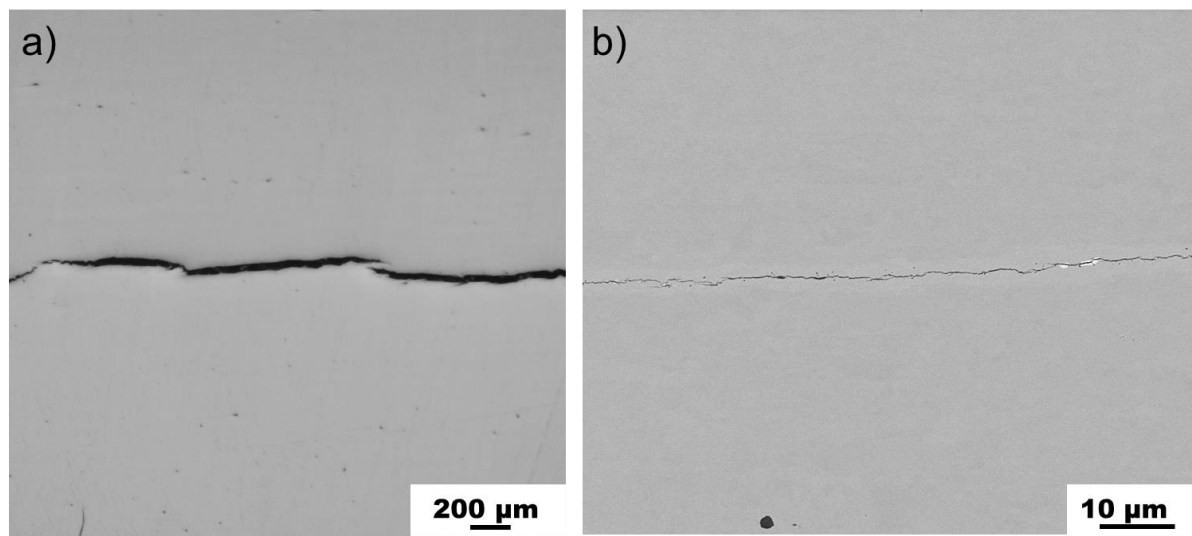

Figure 6: (a) OM and (b) SEM (b) images of one of the HZA and BM, respective samples submitted to the HIC test.

Table 3: HIC test parameters for BM, HAZ, and SZ

Parameters (%)	BM	HAZ	SZ
CLR	41.14	94.14	68.30
CTR	1.68	19.67	4.19
CSR	0.06	5.43	1.94

The type, density, and distribution of non-metallic inclusions and the segregation bands greatly impacted HSLA steel performance in the H_2S environment. Also, the segregation region is the most preferred area for HIC crack propagation [65,66]. When examining the path and crack propagation, irregular inclusions were found. The inclusions were analyzed by EDS, whose spectra show MnS and CaO in Figure 7a-d, AlO inclusions in Figure7e. According to the literature, irregular inclusions act as points of accumulation of hydrogen, consequently

concentrating internal tensions that propitiate the nucleation and propagation of cracks [63–66]. The irregular inclusions are considered irreversible traps where hydrogen atoms are mainly trapped by the interfaces between the inclusions and the steel matrix and initiate micro-cracks under hydrogen charging [66–68].
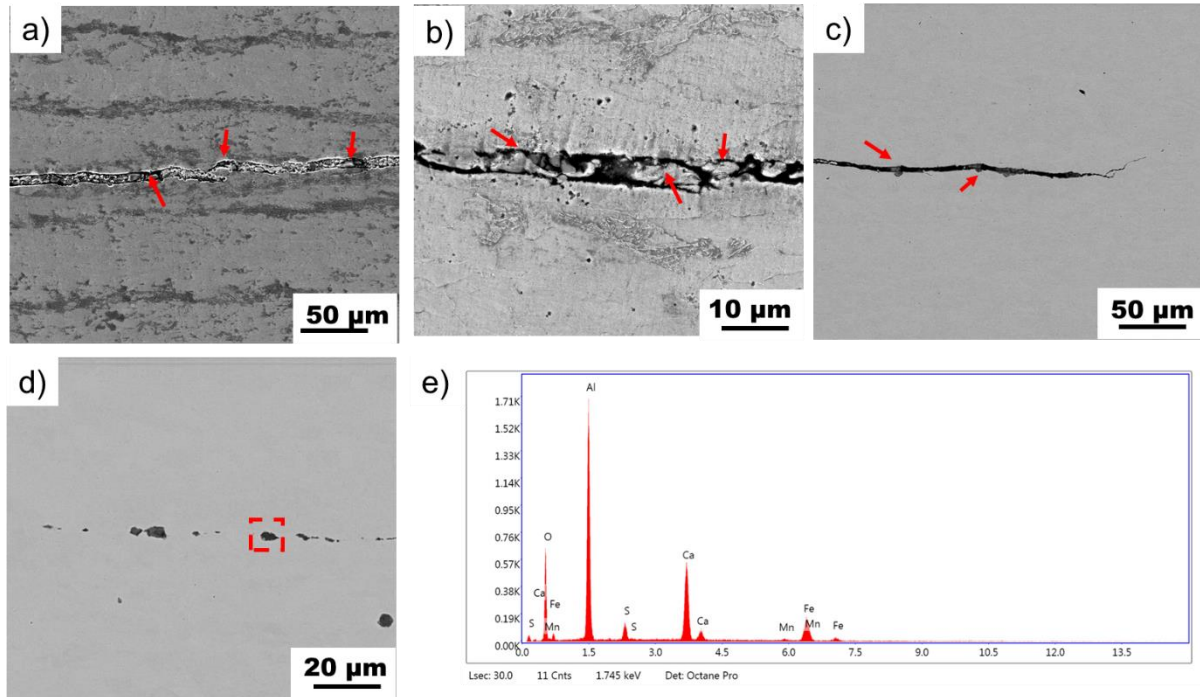

Figure 7: (a) (b) and (c) SEM image of a crack initiating from inclusion, (e) EDS analysis of the inclusion indicated Al-O and MnS inclusion in EDS analysis of the inclusion stated in (d). The red arrow depicts the position of some secondary phases.

A specific region in Figure 7d presents its EDS analysis in Figure 7e, indicating the crack initiation from the Al-O inclusion next to an MnS inclusion. Al oxide inclusions are hard, brittle, and incoherent to the metal matrix, causing micro-voids in the steel matrix interface [69,70]. The cracks are relatively easy to initiate at the boundary between Al-O inclusions and metal [30,62,69,70]. Mostafijur Rahman [34] showed that globular inclusions were less likely to start the crack than spinal and rectangular inclusions. However, HIC crack propagation depends on the distance between inclusions and grain size in the metallic matrix between the inclusions. Two inclusions tend to connect when they are close to each other, accelerating the risk of failure for HIC. Crack nucleation occurs in both inclusions and then propagated between them, creating a longer crack. When the grain size between the inclusions is smaller, the HIC cracks propagate more frequently [34]. It is well known that elongated manganese sulfide inclusions increase the HIC susceptibility by acting as strong traps and nucleation sites for HIC cracks [69,71–73]. The shape of this inclusion and its incoherent with the metal matrix and can provide a region with high-stress concentration [73].

The formation of different microstructural constituents might explain the difference in the HIC resistance in each of the regions analyzed due to the welding process. The HIC crack propagation occurs preferably along with the hard phase [71]. In BM, the crack tended to nucleate and propagate along with the ferrite-pearlite interfaces [71,74], as shown in Figure 8a. The ferrite phase has a high resistance against HIC cracks due to its ductility. The HIC crack propagation comes up more quickly in the pearlitic structure because it is harder than ferrite [71]. Although this region presents inclusions and precipitates, crack initiation locations are composed for the ferritic phase that slows further cracks. Therefore, this region is more resistant to HIC [33,71,72].
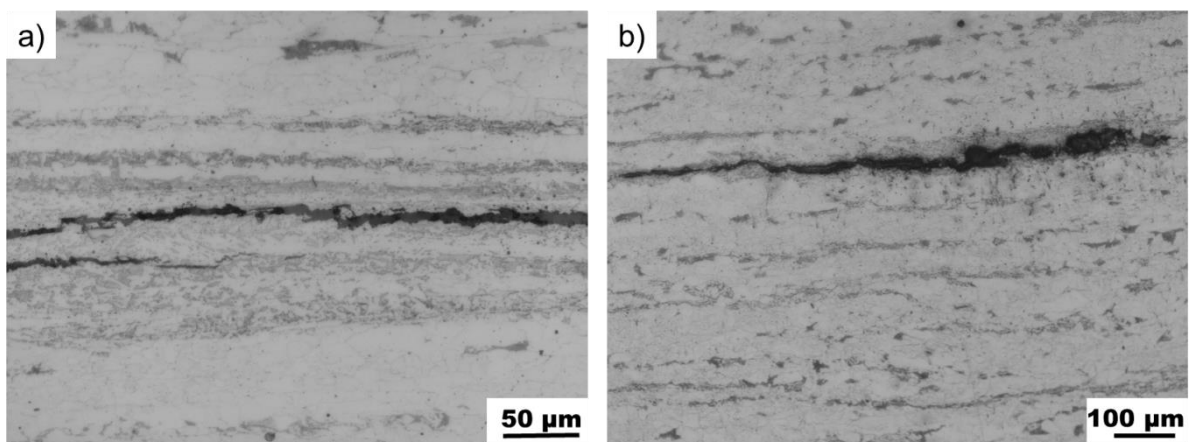

Figure 8: OM image of hydrogen-induced cracking (a) along the ferrite-pearlite interfaces in BM and (b) along with the M/A- ferrite interfaces in SZ.

Among the SZ, the cracks occurred in the RSZ due to the segregation in the mid of the plate thickness. This region is predominantly polygonal ferrite with many secondary phases, mainly bands of M/A. This structure is the hardest phase in steel, being the most susceptible to HIC [33]. As shown in Figure 8b, the crack tended to nucleate in martensite and propagate along with the ferrite interfaces. However, despite the hard M/A microconstituent, the matrix comprises polygonal ferrite and ductile phase, retarding crack propagation [33,71,72]. Laureys et al. [72] report that cracks propagation was favorable along the segregation line of the samples, which consisted of continuous aligned martensitic phases; however, in the propagation path of the crack along with the ferrite phase, the plastic deformation of this softer phase resulted in crack blunting and arrest.

The HAZ-HT is the region with the most HIC susceptibility. One factor influencing these results is the microsctrure of this region, bainite packets with straight ferrite plates, granular bainite, and acicular ferrite. The bainite phase is harder than ferrite, being vulnerable to HIC. The presence of cementite and fine carbides in bainite and lath boundaries is considered a

hydrogen trap [33,75,76]. According to Li et al. [32], the lowest HIC resistance is caused by a large volume fraction of the bainite lath and M/A microconstituents.

Besides the variability in the microstructure and inclusions, the grain boundaries can also influence HIC susceptibility [34,39,77]. The hydrogen traps decrease with the increase in grain size and decrease triple grain boundaries [78], unlike the high fraction of small grains dropping the HIC resistance due to the high grain boundary concentration, providing a path for hydrogen mobility [34]. Figure 5 shows that BM has a large grain size average, influencing a good HIC resistance behavior.

Furthermore, another factor that influences HIC behavior is grain boundary distributions. In which, misorientation angle within the range of $5° < θ < 15°$ were regarded as low angle grain boundary (LAGB), and $15° < θ < 62.5°$ high angle grain boundaries (HAGB). The HAGB are considered preferred places for crack propagation to keep relatively high internal energy. The LAGB due creates good alignment between neighboring grain, slowing crack propagation [38,39]. LAGB, due to their low energy, supply higher resistance to intergranular crack propagation [79]. However, the LAGB was not efficient in retardation or arresting the transgranular crack propagation [4,80]. Nevertheless, some authors report that transgranular cracks did not indicate a clear preferential trend in relation-oriented grains [69]. According toTable 2, the three regions analyzed presented similar grain boundary distributions, not becoming the decisive factor in propagating cracks.

3.3. Electrochemical results

3.3.1. Potentiodynamic polarization

The polarization curves of the BM and regions of the FSWeld in the carbonate–bicarbonate solution are illustrated in Figure 9.
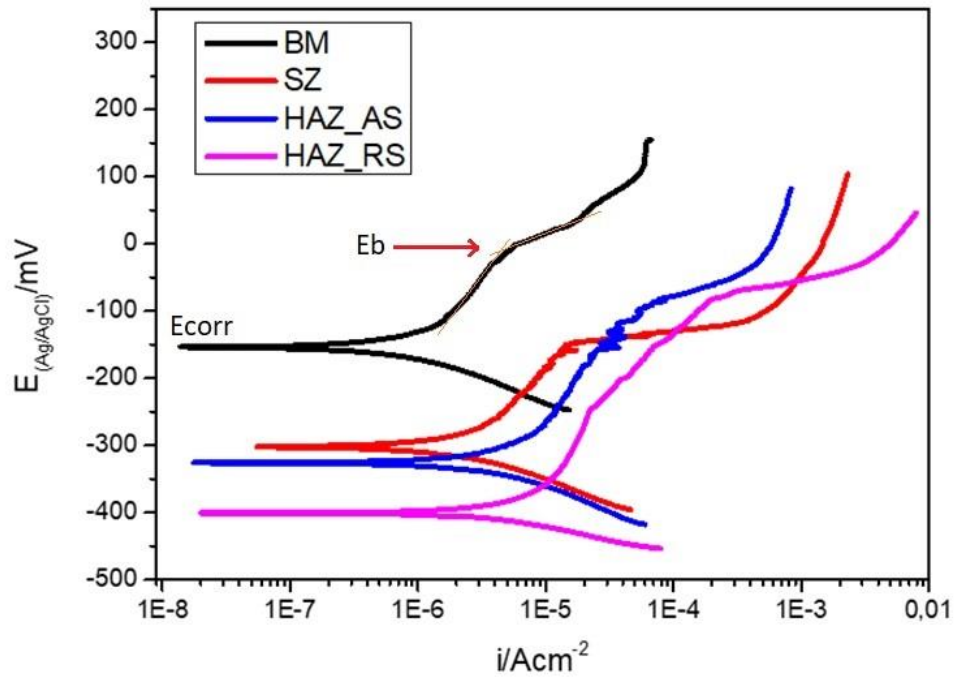
Figure 9: Representative potentiodynamic polarization curves obtained in carbonate–bicarbonate solution for the different FSWeld regions of X70 steel.

The carbon steel within the carbonate/bicarbonate solution occurred the passivity due to the coating of iron carbonate and iron oxide films [22,26,81]. Although the disbanded coating strongly depends on the trapped carbonate/bicarbonate solution concentration, the protective film is formed at any concentration [82]. The passive current density measured in this work is in the order of 10^{-6} to 10^{-4} A/cm^2, as presented in Figure 9. Second, Li et al. [26], in this current of 10^{-7} to 10^{-6} A/cm^2, even being a very little current density, the anodic dissolution is happening. Thus, a passive-like film is formed on the surface. The term ''passive-like'' is used when a current density deceleration occurs. The film formed on the surface is not passive due to current densities more significant than what is typically observed for passive films [13].

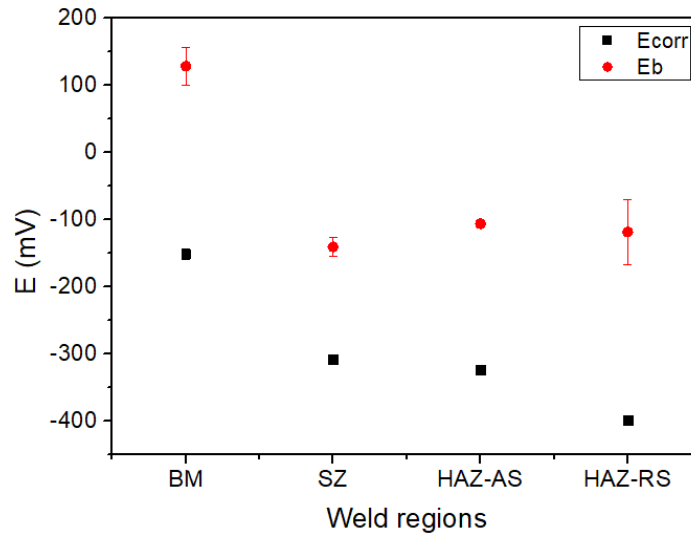The measured corrosion parameters, corrosion potential, Ecorr, and breakdown corrosion are summarized in Figure 10.

Figure 10: Corrosion potentials (Ecorr) and breaking potentials (Eb) of the BM and FSweld regions studied in a carbonate–bicarbonate solution.

Figure 10 shows that the BM region presents the highest corrosion and breakdown potential (Ecorr = −151 mV and Eb = 129 mV). From Ecorr results, it can be confirmed that the HAZ-RS region is more susceptible to corrosion. On the other hand, the Eb results showed similar behavior in the different FSWeld areas with a slight tendency of the SZ region to be more prone to breakdown. The higher breakdown potential in the BM region (Figure 9 and Figure 10) is due to polygonal ferritic and degenerated pearlite banded microstructure. Ferrite-pearlite structure favors a $FeCO_3$ film growth due to carbonate deposits attached better to the steel surface, which occurs because the ferrite inside the pearlitic matrix is undone, carbonate deposit is fixed between the remaining cementite plates exposed to the surface [22].

The Ecorr values of the welded region showed differences between the sub-regions and were lower than BM. This indicates that the microstructure of each region affected the corrosion. The presence of bainite and second phases increases the steel activity and increases the corrosion rate [83].

The Eb in SZ and HAZ is lower than BM, indicating that the broken film is favorable. This behavior occurred because the main microstructure is bainite (composed of bainite packets (BP) and granular bainite (GB). In the bainitic microstructure, the carbide particle distribution is less continuous and less ordered in nature. The carbonate deposit is fixed with less efficiency on the surface of the metal [22]. Thus, the bainitic structures are ineffective in promoting the film on the surface of steel [22,81], such as ferrite. The smaller passive region between the region analysis occurred in SZ due to lower second phase content in their microstructure, as shown in Figure 5. It probably means it has a smaller amount of M/A than other regions. The passive region depends on the M/A content; thus, the lower the amount of the M/A, the lower the passive region [13].

3.1.1. LEIS

Figure 11a shows the LEIS map measured at corrosion potential, and Figure 11b, the scheme of which region of the weld the measurements were made. Y represents the measured admittance amplitude in the x–y–z 3-dimensional space, which usually refers to the individual measuring point electrode stability. The 3-D admittance distribution was also projected on the x–y plane. The color level indicated the admittance magnitude, as shown in the color legend (bluish regions indicate less corrosion susceptibility). The arrow represented the scanning directions that were measured from the retreating side to for advanced side.

The LEIS maps, Figure 11, directly indicate the influences of welding regions on the protective properties of the corrosion product layer generated in surface steel in 24h. It is seen that, generally, there was a smaller admittance value on the retreating side. Thus, it is reasonable to assume higher dissolution in this welding region (close to HZ – Figure 2). The advanced side is generating and depositing more iron carbonate products [26].
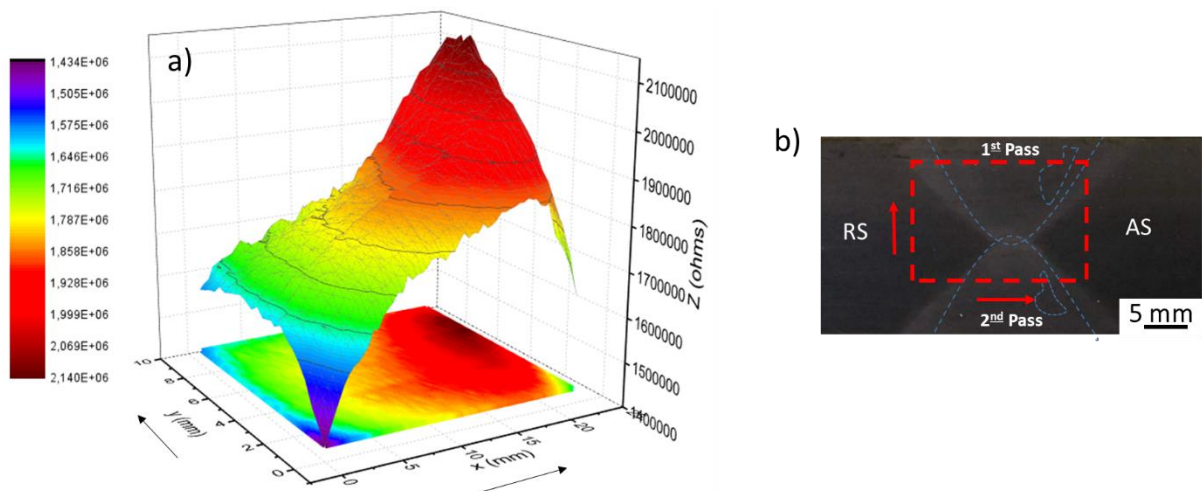

Figure 11: a) LEIS map measured (Y: admittance). b) Scanning area indicated in the carbonate–bicarbonate solution.

The material flow at the advanced side around the tool undergoes highly severe plastic deformation and thermal exposure because of the lower frictional forces. The advanced side peak temperature was slightly higher than that at the retreating side [65,66], possibly created by the hard zone.

The HZ and HAZ have a high rate of secondary phases, Figure 5, which leads to a higher corrosion rate, causing the generating and depositing of more iron carbonate products. The increased number of secondary phases may indicate a high concentration of M/A constituents, leading to a higher passive region [13], suggesting a most stable film.

18

Unlike SZ, it has a grain refining and a second phase decrease, the uniform distribution of the phases leading to inhibition of the corrosion process [19]. The possible smaller amount of M/A indicates a less stable film. Thus, the weld regions formed a galvanic cell that couples SZ and HAZ-RS, which becomes cathodic relative to HZ-HAZ-AS coupling when exposed to the carbonate–bicarbonate solution larger deposit of the iron carbonate product in the advanced side.

4. Conclusions

BM was consisting of a matrix of equiaxial ferritic grains and degenerated pearlite bands that modified to polygonal ferrite in HAZ-LT, bainite with the granular bainite (GB), bainite packets B(P), and acicular ferrite morphology in the HAZ, bainite with the granular bainite (GB), bainite packets B(P) in SZ and HZ. The proportion of B (P) with straight plates is higher in the HZ than the rest of the SZ. Moreover, the RSZ due to the double stirring, resulting in a microstructure predominantly of polygonal ferrite with many secondary phases.

The weld regions were more highly susceptible to HIC than BM, being the most susceptible in HZA-HT. The crack initiation was strongly dependent on the microstructure, in which the crack propagated more easily in hard phases, as the bainite in HZA-TH and the martensite in SZ.

The BM shows better corrosion resistance than the weld region, more positive Eb and Ecorr, bainite, and second phases decreased charge transfer resistance. The microstructure of polygonal ferritic and degenerated pearlite bands in BM fixed the carbonate deposits in surface steel. The weld region had a less passive region than the BM. The SZ presented the bainitic microstructure with such characteristics that caused a less efficient fixed carbonate deposit on the steel surface. Also, the smaller amount of M/A in SZ led to a lower passive region.

The weld regions formed a galvanic cell in which the couple SZ and HAZ-RS, which becomes cathodic relative to the couple HZ-HAZ-AS, is due to grain refining. A second phase decrease inhibits the corrosion process. The possible smaller amount of M/A indicates a less stable film in SZ and a high rate of secondary phases, which leads to a higher rate of corrosion and a high concentration of M/A constituents, indicating a most stable film in HAZ and HZ.

Acknowledgments

Ethical Approval

This research did not involve Human Participants or Animals; thus, ethical approval is not necessary.

Consent to Participate:

This research did not involve Human Participants; thus, consent of participation is not necessary.

Consent to Publish:

This research did not involve Human Participants; thus, Consent to Publish is not necessary.

Authors Contributions:

- J. M. Giarola: Data curation; Formal analysis; Writing – original draft
- J. W. Calderón-Hernández: Investigation; Writing - review & editing.
- J.M Quispe-Avilés: Investigation
- J.A. Avila: Conceptualization; Supervision; Data curation; Formal analysis; Writing
- W. W. Bose Filho: Conceptualization; Supervision; Data curation; Formal analysis; Project administration; Writing

Funding:

Competing Interests:

The authors reported no potential conflict of interest.

Availability of data and materials:

     The data that support the findings of this study are available from the corresponding author, [J.A. Avila], upon reasonable request.

Disclosure statement:

The authors reported no potential conflict of interest.

6. References

[1]   Hashemi SH. Strength-hardness statistical correlation in API X65 steel. Mater Sci Eng A 2011;528:1648–55. https://doi.org/10.1016/j.msea.2010.10.089.

[2]   Soeiro Junior JC, Rocha DB, Brandi SD. Uma breve revisão histórica do desenvolvimento da soldagem dos aços API para tubulações. Soldag Inspeção 2013;18:176–95. https://doi.org/10.1590/S0104-92242013000200011.

[3]   Hoyos JJ, Pereira VF, Giorjao RR, McNelley TR, Ramírez AJ. Effect of friction stir welding on hydrogen content of ISO 3183 X80M steel. J Manuf Process 2016;22:82–9. https://doi.org/10.1016/j.jmapro.2016.01.012.

[4]   Hoyos JJ, Masoumi M, Pereira VF, Tschiptschin AP. Influence of hydrogen on the microstructure and fracture toughness of friction stir welded plates of API 5L X80 pipeline steel. Int J Hydrogen Energy 2019;44:23458–71. https://doi.org/10.1016/j.ijhydene.2019.06.210.

[5]   Ávila JA, Ruchert COFT, Mei PR, Marinho RR, Paes MTP, Ramirez AJ. Fracture toughness assessment at different temperatures and regions within a friction stirred API 5L X80 steel welded plates. Eng Fract Mech 2015;147:176–86. https://doi.org/10.1016/j.engfracmech.2015.08.006.

[6]   Santos TFA, Hermenegildo TFC, Afonso CRM, Marinho RR, Paes MTP, Ramirez AJ. Fracture toughness of ISO 3183 X80M (API 5L X80) steel friction stir welds. Eng Fract Mech 2010;77:2937–45. https://doi.org/10.1016/j.engfracmech.2010.07.022.

[7]   Chludzinski M, Dos Santos RE, Pissanti DR, Kroeff FC, Mattei F, Dalpiaz G, et al. Full-scale friction welding system for pipeline steels. J Mater Res Technol 2019;8:1773–80. https://doi.org/10.1016/j.jmrt.2018.12.007.

[8]   Meyghani B, Awang M. A Comparison Between the Flat and the Curved Friction Stir Welding (FSW) Thermomechanical Behaviour. Arch Comput Methods Eng 2020;27:563–76. https://doi.org/10.1007/s11831-019-09319-x.

[9]   Feng Z, Lim YC, Mahoney M, Sanderson S, Larsen S, Steel R, et al. Flexible Friction Stir Joining Technology. Oak Ridge, TN (United States): 2015. https://doi.org/10.2172/1210157.

[10]   Faes K, Dhooge A, De Baets P, Afschrift P. New friction welding process for pipeline girth welds-welding time optimisation. Int J Adv Manuf Technol 2009;43:982–92. https://doi.org/10.1007/s00170-008-1775-z.

[11]   Marche Bois, H., Letter, J., Orlans-Joliet B. SSC performance of a Super 13%Cr

Martensitic Stainless Steel for OCTG: Three-dimensional itness-for-purpose mapping according to H2S, pH and chloride. NACE Int 2007;07090.

[12]   Shirinzadeh-Dastgiri M, Mohammadi J, Behnamian Y, Eghlimi A, Mostafaei A. Metallurgical investigations and corrosion behavior of failed weld joint in AISI 1518 low carbon steel pipeline. Eng Fail Anal 2015;53:78–96. https://doi.org/10.1016/j.engfailanal.2015.03.015.

[13]   Mohammadi F, Eliyan FF, Alfantazi A. Corrosion of simulated weld HAZ of API X-80 pipeline steel. Corros Sci 2012;63:323–33. https://doi.org/10.1016/j.corsci.2012.06.014.

[14]   Luo J, Luo S, Li L, Zhang L, Wu G, Zhu L. Stress corrosion cracking behavior of X90 pipeline steel and its weld joint at different applied potentials in near-neutral solutions. Nat Gas Ind B 2019;6:138–44. https://doi.org/10.1016/j.ngib.2018.08.002.

[15]   Zhang H, Wang D, Xue P, Wu LH, Ni DR, Ma ZY. Microstructural evolution and pitting corrosion behavior of friction stir welded joint of high nitrogen stainless steel. Mater Des 2016;110:802–10. https://doi.org/10.1016/j.matdes.2016.08.048.

[16]   Fujii H, Cui L, Tsuji N, Maeda M, Nakata K, Nogi K. Friction stir welding of carbon steels. Mater Sci Eng A 2006;429:50–7. https://doi.org/10.1016/j.msea.2006.04.118.

[17]   Sato YS, Shiota A, Kokawa H, Okamoto K, Yang Q, Kim C. Effect of interfacial microstructure on lap shear strength of friction stir spot weld of aluminium alloy to magnesium alloy. Sci Technol Weld Join 2010;15:319–24. https://doi.org/10.1179/136217109X12568132624208.

[18]   Sarlak H, Atapour M, Esmailzadeh M. Corrosion behavior of friction stir welded lean duplex stainless steel. Mater Des 2015;66:209–16. https://doi.org/10.1016/j.matdes.2014.10.060.

[19]   da Cruz JR, Bertazzoli R. Characterization of Corrosion Within Friction Stir Weld Zones of an API X-70 Steel Using a Novel Microcell Setup. J Mater Eng Perform 2020;29:98–108. https://doi.org/10.1007/s11665-019-04531-z.

[20]   Sekban DM, Aktarer SM, Purcek G. Friction Stir Welding of Low-Carbon Shipbuilding Steel Plates: Microstructure, Mechanical Properties, and Corrosion Behavior. Metall Mater Trans A 2019;50:4127–40. https://doi.org/10.1007/s11661-019-05324-8.

[21]   Giarola JM, Calderón-Hernández JW, Conde FF, Marcomini JB, de Melo HG, Avila JA, et al. Corrosion Behavior and Microstructural Characterization of Friction Stir Welded API X70 Steel. J Mater Eng Perform 2021;00:00. https://doi.org/10.1007/s11665-021-05640-4.

[22]   Khalaj G, Khalaj MJ. Investigating the corrosion of the Heat-Affected Zones (HAZs) of API-X70 pipeline steels in aerated carbonate solution by electrochemical methods. Int J Press Vessel Pip 2016;145:1–12. https://doi.org/10.1016/j.ijpvp.2016.06.001.

[23]   Moon K-M, Lee M-H, Kim K-J, Kim S-J. The effect of post-weld heat treatment affecting corrosion resistance and hydrogen embrittlement of HAZ part in FCAW. Surf Coatings Technol 2003;169–170:675–8. https://doi.org/10.1016/s0257-8972(03)00060-4.

[24]   Zhang GA, Cheng YF. Micro-electrochemical characterization of corrosion of welded X70 pipeline steel in near-neutral pH solution. Corros Sci 2009;51:1714–24. https://doi.org/10.1016/j.corsci.2009.04.030.

[25]   Hemmingsen T, Hovdan H, Sanni P, Aagotnes NO. The influence of electrolyte reduction potential on weld corrosion. Electrochim Acta 2002;47:3949–55. https://doi.org/10.1016/S0013-4686(02)00366-3.

[26]   Li MC, Cheng YF. Corrosion of the stressed pipe steel in carbonate – bicarbonate solution studied by scanning localized electrochemical impedance spectroscopy 2008;53:2831–6. https://doi.org/10.1016/j.electacta.2007.10.077.

[27]   Behjat A, Shamanian M, Atapour M, Sarmadi MA. Microstructure and Corrosion Properties of Friction Stir-Welded High-Strength Low -Alloy Steel. Trans Indian Inst Met 2021. https://doi.org/10.1007/s12666-021-02219-4.

[28]   Husain M, Meena L, Ghosh M, Prabhu N. Corrosion at the Weld Nugget of the

Friction-Stir-Welded Medium Strength Steel: Effect of Microstructure. Metall Mater Trans A 2021;52:2642–56. https://doi.org/10.1007/s11661-021-06257-x.

[29]   Mohtadi-Bonab MA, Szpunar JA, Razavi-Tousi SS. A comparative study of hydrogen induced cracking behavior in API 5L X60 and X70 pipeline steels. Eng Fail Anal 2013;33:163–75. https://doi.org/10.1016/j.engfailanal.2013.04.028.

[30]   Xue HB, Cheng YF. Characterization of inclusions of X80 pipeline steel and its correlation with hydrogen-induced cracking. Corros Sci 2011;53:1201–8. https://doi.org/10.1016/j.corsci.2010.12.011.

[31]   Dong CF, Liu ZY, Li XG, Cheng YF. Effects of hydrogen-charging on the susceptibility of X100 pipeline steel to hydrogen-induced cracking. Int J Hydrogen Energy 2009;34:9879–84. https://doi.org/10.1016/j.ijhydene.2009.09.090.

[32]   Li J, Gao X, Du L, Liu Z. Relationship between microstructure and hydrogen induced cracking behavior in a low alloy pipeline steel. J Mater Sci Technol 2017;33:1504–12. https://doi.org/10.1016/j.jmst.2017.09.013.

[33]   Mohtadi-Bonab MA, Szpunar JA, Collins L, Stankievech R. Evaluation of hydrogen induced cracking behavior of API X70 pipeline steel at different heat treatments. Int. J. Hydrogen Energy, vol. 39, Elsevier Ltd; 2014, p. 6076–88. https://doi.org/10.1016/j.ijhydene.2014.01.138.

[34]   Mostafijur Rahman KM, Mohtadi-bonab MA, Ouellet R, Szpunar J, Zhu N. Effect of electrochemical hydrogen charging on an API X70 pipeline steel with focus on characterization of inclusions. Int J Press Vessel Pip 2019;173:147–55. https://doi.org/10.1016/j.ijpvp.2019.05.006.

[35]   Khalili Tabas AA, Beidokhti B, Kiani-Rashid AR. Comprehensive study on hydrogen induced cracking of electrical resistance welded API X52 pipeline steel. Int J Hydrogen Energy 2021;46:1012–22. https://doi.org/10.1016/j.ijhydene.2020.09.219.

[36]   Hejazi D, Haq AJ, Yazdipour N, Dunne DP, Calka A, Barbaro F, et al. effect of manganese content and microstructure on the susceptibility of X70 pipeline steel to hydrogen cracking. Mater Sci Eng A 2012;551:40–9. https://doi.org/10.1016/j.msea.2012.04.076.

[37]   Han YD, Wang RZ, Jing HY, Zhao L, Xu LY, Xin P. Sulphide stress cracking behaviour of the coarse-grained heat-affected zone in X100 pipeline steel under different heat inputs. Int J Hydrogen Energy 2020;45:20094–105. https://doi.org/10.1016/j.ijhydene.2020.05.092.

[38]   Ohaeri E, Szpunar J, Fazeli F, Arafin M. Hydrogen induced cracking susceptibility of API 5L X70 pipeline steel in relation to microstructure and crystallographic texture developed after different thermomechanical treatments. Mater Charact 2018;145:142–56. https://doi.org/10.1016/j.matchar.2018.08.034.

[39]   Masoumi M, Silva CC, Béreš M, Ladino DH, de Abreu HFG. Role of crystallographic texture on the improvement of hydrogen-induced crack resistance in API 5L X70 pipeline steel. Int J Hydrogen Energy 2017;42:1318–26. https://doi.org/10.1016/j.ijhydene.2016.10.124.

[40]   Sun Y, Fujii H. Improved resistance to hydrogen embrittlement of friction stir welded high carbon steel plates. Int J Hydrogen Energy 2015;40:8219–29. https://doi.org/10.1016/j.ijhydene.2015.04.070.

[41]   Gan L, Huang F, Zhao X, Liu J, Cheng YF. Hydrogen trapping and hydrogen induced cracking of welded X100 pipeline steel in H2S environments. Int J Hydrogen Energy 2018;43:2293–306. https://doi.org/10.1016/j.ijhydene.2017.11.155.

[42]   Kang Y, Kim M, Kim G, Kim N, Song S. Characteristics of Susceptible Microstructure for Hydrogen-Induced Cracking in the Coarse-Grained Heat-Affected Zone of Carbon Steel. Metall Mater Trans A Phys Metall Mater Sci 2020;51:2143–53. https://doi.org/10.1007/s11661-020-05671-x.

[43]   NACE TM0284. Standard Test Method Evaluation of Pipeline and Pressure Vessel Steels for Resistance to Hydrogen-Induced Cracking. 2011.

[44]   Avila JA, Conde FF, Pinto HC, Rodriguez JF, Grijalba FAF. Microstructural and

Residuals Stress Analysis of Friction Stir Welding of X80 Pipeline Steel Plates Using Magnetic Barkhausen Noise. J Nondestruct Eval 2019;38:86. https://doi.org/10.1007/s10921-019-0625-2.

[45] Avila JA, Escobar JD, Cunha B, Magalhães W, Mei P, Rodriguez J, et al. Physical simulation as a tool to understand friction stir processed X80 pipeline steel plate complex microstructures. J Mater Res Technol 2019;8:1379–88. https://doi.org/10.1016/j.jmrt.2018.09.009.

[46] Avila JA, Rodriguez J, Mei PR, Ramirez AJ. Microstructure and fracture toughness of multipass friction stir welded joints of API-5L-X80 steel plates. Mater Sci Eng A 2016;673:257–65. https://doi.org/10.1016/j.msea.2016.07.045.

[47] Zajac S, Schwinn V, Tacke KH. Characterisation and Quantification of Complex Bainitic Microstructures in High and Ultra-High Strength Linepipe Steels. Mater Sci Forum 2009;500–501:387–94. https://doi.org/10.4028/www.scientific.net/msf.500-501.387.

[48] Osipov N, Gourgues-Lorenzon AF, Marini B, Mounoury V, Nguyen F, Cailletaud G. FE modelling of bainitic steels using crystal plasticity. Philos Mag 2008;88:3757–77. https://doi.org/10.1080/14786430802566380.

[49] Wang W, Xu R, Hao Y, Wang Q, Yu L, Che Q, et al. Corrosion fatigue behavior of friction stir processed interstitial free steel. J Mater Sci Technol 2018;34:148–56. https://doi.org/10.1016/j.jmst.2017.11.013.

[50] Nafisi S, Arafin MA, Collins L, Szpunar J. Texture and mechanical properties of API X100 steel manufactured under various thermomechanical cycles. Mater Sci Eng A 2012;531:2–11. https://doi.org/10.1016/j.msea.2011.09.072.

[51] Gao Q, Lu C, Li H, Li J, Han J, Chen L. Anisotropy and microstructural evolutions of X70 pipeline steel during tensile deformation. J Mater Res 2018;33:3512–20. https://doi.org/10.1557/jmr.2018.190.

[52] Díaz-Fuentes M, Iza-Mendia A, Gutiérrez I. Analysis of Different Acicular Ferrite Microstructures in Low-Carbon Steels by Electron Backscattered Diffraction . Study of Their Toughness Behavior. Metall Mater Trans A 2003;34A:2505–16.

[53] Gurova T, Gomes LS, Peripolli SB, Chavez GFS, Estefen SF, Leontiev A. Misorientation changes and residual stresses redistribution after welding. A physical simulation. Mater Res 2019;22. https://doi.org/10.1590/1980-5373-MR-2019-0360.

[54] Odnobokova M, Belyakov A, Kaibyshev R. Development of nanocrystalline 304L stainless steel by large strain cold working. Metals (Basel) 2015;5:656–68. https://doi.org/10.3390/met5020656.

[55] Shakhova I, Dudko V, Belyakov A, Tsuzaki K, Kaibyshev R. Effect of large strain cold rolling and subsequent annealing on microstructure and mechanical properties of an austenitic stainless steel. Mater Sci Eng A 2012;545:176–86. https://doi.org/10.1016/j.msea.2012.02.101.

[56] Shrestha SL, Breen AJ, Trimby P, Proust G, Ringer SP, Cairney JM. An automated method of quantifying ferrite microstructures using electron backscatter diffraction (EBSD) data. Ultramicroscopy 2014;137:40–7. https://doi.org/10.1016/j.ultramic.2013.11.003.

[57] Kang JS, Seol JB, Park CG. Three-dimensional characterization of bainitic microstructures in low-carbon high-strength low-alloy steel studied by electron backscatter diffraction. Mater Charact 2013;79:110–21. https://doi.org/10.1016/j.matchar.2013.02.009.

[58] Park K, Hwang SW, Ji JH, Lee CH. Inclusions Nucleating Intragranular Polygonal Ferrite and Acicular Ferrite in Low Alloyed Carbon Manganese Steel Welds 2011;17:349–56. https://doi.org/10.1007/s12540-011-0425-4.

[59] Mandal S, Tewary NK, Ghosh SK, Chakrabarti D, Chatterjee S. Thermo-mechanically controlled processed ultrahigh strength steel: Microstructure, texture and mechanical properties. Mater Sci Eng A 2016;663:126–40. https://doi.org/10.1016/j.msea.2016.03.127.

[60] Zhu K, Bouaziz O, Oberbillig C, Huang M. An approach to define the effective lath size controlling yield strength of bainite. Mater Sci Eng A 2010;527:6614–9. https://doi.org/10.1016/j.msea.2010.06.061.

[61] Flower HM, Lindley TC. Electron backscattering diffraction study of acicular ferrite, bainite, and martensite steel microstructures. Mater Sci Technol 2000;16:26–40. https://doi.org/10.1179/026708300773002636.

[62] Jin TY, Liu ZY, Cheng YF. Effect of non-metallic inclusions on hydrogen-induced cracking of API5L X100 steel. Int J Hydrogen Energy 2010;35:8014–21. https://doi.org/10.1016/j.ijhydene.2010.05.089.

[63] Dong CF, Li XG, Liu ZY, Zhang YR. Hydrogen-induced cracking and healing behaviour of X70 steel 2009;484:966–72. https://doi.org/10.1016/j.jallcom.2009.05.085.

[64] Quispe-Avilés JM, Hincapie-Ladino D, Falleiros NA, Melo HG de. A Comparative Investigation of the Corrosion Resistance and HIC Suceptibility of API 5L X65 and API 5L X80 Steels. Mater Res 2019;22:1–13. https://doi.org/10.1590/1980-5373-mr-2018-0191.

[65] Qu J, Feng M, An T, Bi Z, Du J, Yang F, et al. Hydrogen-assisted crack growth in the heat-affected zone of X80 steels during in situ hydrogen charging. Materials (Basel) 2019;12:1–15. https://doi.org/10.3390/ma12162575.

[66] Ånmark N, Karasev A, Jönsson PG. The effect of different non-metallic inclusions on the machinability of steels. Materials (Basel) 2015;8:751–83. https://doi.org/10.3390/ma8020751.

[67] Masoumi M, Silva CC, Ferreira H, Abreu G De. Effect of crystallographic orientations on the hydrogen-induced cracking resistance improvement of API 5L X70 pipeline steel under various thermomechanical processing. Eval Program Plann 2016;111:121–31. https://doi.org/10.1016/j.corsci.2016.05.003.

[68] Du XS, Cao WB, Wang CD, Li SJ, Zhao JY, Sun YF. Effect of microstructures and inclusions on hydrogen-induced cracking and blistering of A537 steel. Mater Sci Eng A 2015;642:181–6. https://doi.org/10.1016/j.msea.2015.06.085.

[69] Mohtadi-Bonab MA, Eskandari M, Karimdadashi R, Szpunar JA. Effect of different microstructural parameters on hydrogen induced cracking in an API X70 pipeline steel. Met Mater Int 2017;23:726–35. https://doi.org/10.1007/s12540-017-6691-z.

[70] Liu ZY, Li XG, Du CW, Lu L, Zhang YR, Cheng YF. Effect of inclusions on initiation of stress corrosion cracks in X70 pipeline steel in an acidic soil environment. Corros Sci 2009;51:895–900. https://doi.org/10.1016/j.corsci.2009.01.007.

[71] Mohtadi-bonab MA, Eskandari M. A focus on different factors affecting hydrogen induced cracking in oil and natural gas pipeline steel. Eng Fail Anal 2017;79:351–60. https://doi.org/10.1016/j.engfailanal.2017.05.022.

[72] Laureys A, Pinson M, Claeys L, De Seranno T, Depover T, Verbeken K. Initiation of hydrogen induced cracks at secondary phase particles. Frat Ed Integrita Strutt 2020;14:113–27. https://doi.org/10.3221/IGF-ESIS.52.10.

[73] Mohtadi-Bonab MA, Mousavi H, Pourazizi R, Szpunar JA. Finite element modeling of HIC propagation in pipeline steel with regard to experimental observations. Int J Hydrogen Energy 2020;45:23122–33. https://doi.org/10.1016/j.ijhydene.2020.06.054.

[74] Wasim M, Djukic MB. Hydrogen embrittlement of low carbon structural steel at macro-, micro- and nano-levels. Int J Hydrogen Energy 2019;45:2145–56. https://doi.org/10.1016/j.ijhydene.2019.11.070.

[75] Huang F, Liu J, Deng ZJ, Cheng JH, Lu ZH, Li XG. Effect of microstructure and inclusions on hydrogen induced cracking susceptibility and hydrogen trapping efficiency of X120 pipeline steel. Mater Sci Eng A 2010;527:6997–7001. https://doi.org/10.1016/j.msea.2010.07.022.

[76] Arafin MA, Szpunar JA. Effect of bainitic microstructure on the susceptibility of pipeline steels to hydrogen induced cracking. Mater Sci Eng A 2011;528:4927–40. https://doi.org/10.1016/j.msea.2011.03.036.

[77] Li L, Song B, Cheng J, Yang Y, Liu Z. Effects of cooling processes on microstructure and susceptibility of hydrogen-induced cracking of X80 pipeline steel. Mater Corros 2018;69:590–600. https://doi.org/10.1002/maco.201709703.

[78] Thomas A, Szpunar JA. Hydrogen diffusion and trapping in X70 pipeline steel. Int J Hydrogen Energy 2019;45:2390–404. https://doi.org/10.1016/j.ijhydene.2019.11.096.

[79] Venegas V, Caleyo F, González JL, Baudin T, Hallen JM, Penelle R. EBSD study of hydrogen-induced cracking in API-5L-X46 pipeline steel. Scr Mater 2005;52:147–52. https://doi.org/10.1016/j.scriptamat.2004.09.015.

[80] Saleh AA, Hejazi D, Gazder AA, Dunne DP, Pereloma E V. Investigation of the effect of electrolytic hydrogen charging of X70 steel : II . Microstructural and crystallographic analyses of the formation of hydrogen induced cracks and blisters. Int J Hydrogen Energy 2016;41:12424–35. https://doi.org/10.1016/j.ijhydene.2016.05.235.

[81] Bordbar S, Alizadeh M, Hashemi SH. Effects of microstructure alteration on corrosion behavior of welded joint in API X70 pipeline steel. Mater Des 2013;45:597–604. https://doi.org/10.1016/j.matdes.2012.09.051.

[82] Fu AQ, Cheng YF. Electrochemical polarization behavior of X70 steel in thin carbonate/bicarbonate solution layers trapped under a disbonded coating and its implication on pipeline SCC. Corros Sci 2010;52:2511–8. https://doi.org/10.1016/j.corsci.2010.03.019.

[83] Du CW, Li XG, Liang P, Liu ZY, Jia GF, Cheng YF. Effects of Microstructure on Corrosion of X70 Pipe Steel in an Alkaline Soil 2009;18:216–20. https://doi.org/10.1007/s11665-008-9280-y.